UCLA
UCLA Previously Published Works

Title

Motion-robust quantitative multiparametric brain MRI with motion-resolved MR multitasking

Permalink

https://escholarship.org/uc/item/10z587hb

Journal

Magnetic Resonance in Medicine, 87(1)

ISSN

0740-3194

Authors

Ma, Sen
Wang, Nan
Xie, Yibin
et al.

Publication Date

2022

DOI

10.1002/mrm.28959

Peer reviewed

Motion-Robust Quantitative Multiparametric Brain MRI with Motion-Resolved MR Multitasking

Sen Ma[1], **Nan Wang**[1], **Yibin Xie**[1], **Zhaoyang Fan**[1,2], **Debiao Li**[1], **Anthony G. Christodoulou**[1,*]

[1.]Biomedical Imaging Research Institute, Cedars-Sinai Medical Center, Los Angeles, CA, USA

[2.]Department of Radiology, Keck School of Medicine, University of Southern California, Los Angeles, CA, USA

Abstract

Purpose: To address head motion in brain MRI with a novel motion-resolved imaging framework, with application to motion-robust quantitative multiparametric mapping.

Methods: MR Multitasking conceptualizes the underlying multiparametric image in the presence of motion as a multidimensional low-rank tensor. By incorporating a motion-state dimension into the parameter dimensions and introducing unsupervised motion-state binning and outlier motion reweighting mechanisms, the brain motion can be readily resolved for motion-robust quantitative imaging. A numerical motion phantom was used to simulate different discrete and periodic motion patterns under various translational and rotational scenarios, as well as investigate the sensitivity to exceptionally small and large displacements. In vivo brain MRI was performed to also evaluate different real discrete and periodic motion patterns. The effectiveness of motion-resolved imaging for simultaneous T1/T2/T1ρ mapping in the brain was investigated.

Results: For all 14 simulation scenarios of small, intermediate, and large motion displacements, the motion-resolved approach produced T1/T2/T1ρ maps with less absolute difference errors against the ground truth, lower RMSE and higher SSIM of T1/T2/T1ρ measurements compared to motion-removal and no motion handling. For in vivo experiments, the motion-resolved approach produced T1/T2/T1ρ maps with the best image quality free from motion artifacts under random discrete motion, tremor, periodic shaking and nodding patterns, compared to motion-removal and no motion handling. The proposed method also yielded T1/T2/T1ρ measurement distributions closest to the motion-free reference, with minimal measurement bias and variance.

Conclusion: Motion-resolved quantitative brain imaging is achieved with Multitasking, which is generalizable to various head motion patterns without explicit need for registration-based motion correction.

*Corresponding author: Anthony G. Christodoulou, 8700 Beverly Blvd, PACT 400, Los Angeles, CA 90048, anthony.christodoulou@cshs.org, phone: 3104236754.

Keywords

Motion-resolved imaging; Motion-robust; Quantitative multiparametric mapping; Brain MRI; MR Multitasking

1. Introduction

Motion is one of the most challenging issues in clinical brain MRI, especially for the elderly or those with specific neurological syndromes (i.e., Parkinson's disease and epilepsy). In fact, nearly 30% of inpatient MR scans were found to suffer from motion artifacts[1]. Intra-scan motion causes blurring and ghosting artifacts that may lead to a loss of valuable diagnostic information, whereas inter-scan motion produces misaligned images that pose challenges for clinical interpretation. The most common strategy to deal with motion is reacquisition, but it greatly lengthens the scan time, costing approximately $115,000 per scanner per year for hospitals[1]. Other approaches to handling brain motion include the use of external hardware such as an optical tracking system[2] and active marker headband[3], navigator- and image-based motion tracking[4-6], prospective motion correction[4,7], and retrospective motion correction[4,8,9]. However, despite all these efforts, there is still no single method generalizable enough to tackle all the motion issues, but rather a toolbox of partial solutions depending on specific imaging experiments and motion types[10].

Multiparametric mapping techniques, which quantify relaxation (e.g., T1/T2/T2*/QSM/T1ρ), diffusion (e.g., ADC), perfusion and vascular permeability parameters, among others, measure imaging biomarkers with complementary tissue information for early detection, diagnosis, and treatment monitoring of various diseases. However, these techniques are especially prone to motion due to the lengthy scan times and need for multiple image sets, limiting their applicability in clinical practice. Head fixation with cushions has been used to reduce motion during mapping sequences[11], but doesn't completely eliminate motion. The impact of motion on multiparametric maps has been investigated in the context of MR fingerprinting (MRF)[12], where motion robustness has been found to vary with the timing and type of motion. For example, 2D MRF with data rejection and motion correction have both shown limitations in handling through-plane motion[13,14]. Motion robustness and motion correction have been investigated for 3D MRF but are either limited to the very early part of data acquisition[15] or abrupt motion only[16].

In recent years, motion-resolved imaging has drawn significant interests as a novel approach for motion handling. XD-GRASP groups continuously acquired radial spokes into multiple cardiac and/or respiratory motion states, thus introducing extra motion dimensions along which the first-order finite differences between adjacent motion states is exploited for multidimensional image reconstruction[17]. Our group recently developed a multidimensional imaging framework named MR Multitasking, which allows for simultaneous acquisition of multiple tissue parameters by conceptualizing each parameter as a different "time dimension"[18]. This framework has inherent advantages for handling motion, as motion-related time dimensions can be included in addition to the parameter dimensions, thus achieving motion-resolved quantitative imaging by exploring multidimensional signal

correlation along and across different time dimensions (including tissue parameter dimensions and motion dimensions). Elastic physiological motion (e.g., cardiac contraction and dilation, respiration) can be resolved in moving organs, enabling ECG-free, free-breathing T1, T2, and ECV mapping in the heart[18,19], and free-breathing whole-abdomen DCE imaging[20]. In organs with less motion such as carotid arteries, breast, and brain, abrupt motion detection and motion rejection have also been efficiently incorporated into this[21-24]. No external motion-monitoring devices are required with this framework.

In this work, we propose to handle head motion in brain MRI in a motion-resolved manner extending our previously proposed Multitasking approach for motion-resolved cardiac imaging[18] to brain simultaneous T1, T2, and T1ρ quantification[22], showing that motion-resolving with Multitasking is generalizable to other tissue parameter combinations and organs such as the brain, where self-gated motion-resolved imaging is often overlooked as a viable technique. Unlike spontaneous physiological motion, head motion could potentially be more complicated with various distinct patterns. We demonstrate that the proposed solution is generalizable to translation, rotation, discrete motion, and periodic motion without explicit need for image registration-based motion correction. By incorporating a motion-dedicated dimension and multiple parameter dimensions into this multidimensional framework, alongside unsupervised motion-state clustering and outlier reweighting, brain motion can be readily resolved for motion-robust quantitative imaging by modeling the signal correlation along this motion-dedicated dimension (i.e., between different motion states). A numerical motion phantom is used to investigate both discrete motion and periodic motion under different translational and rotational motion scenarios. In vivo experiments are also performed for both discrete and periodic motion patterns.

2. Methods

2.1. Image model

We represent an multiparametric MR image as $x(\mathbf{r}, t_1, t_2, \ldots, t_N, s)$, a multidimensional function of spatial location $\mathbf{r} = [x,y,z]$, motion-state index s, and N time-varying sequence variables t_i with $i = 1,2, \ldots, N$ encoding different tissue parameters (i.e., T1/T2/T2*/T1ρ/ADC, etc.). The "time dimensions" s and $\{t_i\}_{i=1}^N$ both vary with real elapsed time t during the experiment as $s(t)$ and $\{t_i(t)\}_{i=1}^N$, but we will suppress their time dependence for notional simplicity unless otherwise required.

Due to multidimensional spatiotemporal correlation, x can be efficiently represented in low dimensional subspaces through partial separability of space and each of the "time dimensions" s and $\{t_i\}_{i=1}^N$ [25-27]:

$$x(\mathbf{r}, t_1, t_2, \ldots, t_N, s) = \sum_{j=1}^J u_j(\mathbf{r}) \varphi_j(t_1, t_2, \ldots, t_N, s) \tag{1}$$

$$\varphi_j(t_1, t_2, \ldots, t_N, s) = \sum_{j=1}^J \sum_{l_1=1}^{L_1} \cdots \sum_{l_N=1}^{L_N} \sum_{k=1}^K c_{jl_1 \ldots l_N k} v_{1, l_1}(t_1) \ldots v_{N, l_N}(t_N) z_k(s) \tag{2}$$

where $\{u_j(\mathbf{r})\}_{j=1}^{J}$ are spatial basis functions, $c_{jl_1...l_Nk}$ are the elements of a core tensor $\mathscr{C}$, $\{v_{i,l_i}(t_i)\}_{i=1, l_i=1}^{N, L_i}$ are N sets of temporal basis functions with respect to each parameter dimension, $\{z_k(s)\}_{k=1}^{K}$ are temporal basis functions describing motion, and $\{\varphi_j(t_1, t_2, ..., t_N, s)\}_{j=1}^{J}$ spans the multidimensional temporal subspace comprising all the dynamic processes.

The image function x can be rearranged into an (N+2)-way tensor $\mathscr{X}$ with elements $X_{m_1 m_2...m_{N+2}} = x(\mathbf{r}_{m_1}, t_{m_2}, ..., t_{m_{N+1}}, s_{m_{N+2}})$. $\mathscr{X}$ is a low-rank tensor (LRT) according to eqs. (1-2) whose structure can be explicitly expressed in the matrix form of the Tucker tensor decomposition[28]:

$$\mathbf{X}_{(1)} = \mathbf{U}\mathbf{\Phi} \tag{3}$$

$$\mathbf{\Phi} = \mathbf{C}_{(1)}(\mathbf{Z} \otimes \mathbf{V}_N \otimes ... \otimes \mathbf{V}_1)^T \tag{4}$$

where $\mathbf{X}_{(1)}$ and $\mathbf{C}_{(1)}$ are the mode-1 unfolding of $\mathscr{X}$ and $\mathscr{C}$, $\mathbf{U}$ is the spatial factor matrix, $\mathbf{Z}$ and $\{\mathbf{V}_i\}_{i=1}^{N}$ are temporal factor matrices whose rows are temporal basis functions that span the respective temporal subspaces, $\mathbf{\Phi}$ is the combined multidimensional temporal factor matrix, and $\otimes$ stands for the Kronecker product.

We specifically note that in this framework, head motion is modeled with the motion-dedicated time dimension, and is represented with basis functions $\{z_k(s)\}_{k=1}^{K}$ in a low-dimensional subspace. Motion-resolved imaging is thus achieved by modeling the signal correlation between different motion states along this motion-dedicated dimension, without the need for image registration-based motion correction between different motion states in the sense of deformation, translation, and rotation.

2.2. Sequence and sampling strategy for Multitasking quantitative imaging

Many pulse sequences are compatible with the Multitasking framework for simultaneous multiparametric mapping. The most common sequences are magnetization preparation-based (i.e., T2-preparation, T1ρ-preparation, diffusion-preparation, etc.) saturation recovery or inversion recovery sequences[18-24]. Fast low angle shot (FLASH) readouts fill the recovery period between two preparations. K-space data are continuously collected and the entire dataset of k-space lines can be seen as the union of two non-overlapping subsets: 1) auxiliary training data $\mathbf{D}_{tr}$ are periodically collected every a few readouts either at the center k-space line for Cartesian sampling, or using the 0° spoke for radial sampling for motion identification and the estimation of $\mathbf{\Phi}$;[18-24] 2) the rest of the k-space lines belongs to imaging data $\mathbf{D}_{img}$, which traverses the entire k-space with either Gaussian-density random Cartesian trajectory or stack-of-stars trajectory for the estimation of $\mathbf{U}$[18-24].

2.3. Image reconstruction

Motion-resolved imaging is achieved following four stages serially (Figure 1).

2.3.1. Single-time 3D navigator (3DNAV) image reconstruction—Prior to

forming the multidimensional image $x(\mathbf{r}, t_1, t_2, \ldots, t_N, s)$, we reconstruct a time-resolved 3D navigator (3DNAV) image $x_{rt}(\mathbf{r},t)$ with only a single elapsed time dimension t. $x_{rt}(\mathbf{r},t)$ displays the MR image as it occurred in "real-time" during the scan and is related to the multidimensional image as $x_{rt}(\mathbf{r},t) = x(\mathbf{r}(t), t_1(t), t_2(t), \ldots, t_N(t), s(t))$. With only a single time dimension t, the LRT model is reduced to $\mathbf{X}_{rt} = \mathbf{U}_{rt}\mathbf{\Phi}_{rt}$ where $\mathbf{\Phi}_{rt}$ contains the real-time temporal basis functions, and $\mathbf{U}_{rt}$ is the real-time spatial factor matrix. The images in $\mathbf{X}_{rt}$ contain a mixture of different image dynamics (relaxation/diffusion/motion, etc.), which will then be used for motion identification and clustering, and can be reconstructed using a low-rank matrix imaging strategy[27]:

$$\widehat{\mathbf{U}_{rt}} = \arg\min_{\mathbf{U}_{rt}} \|\mathbf{D}_{img} - \Omega(\mathbf{FSU}_{rt}\mathbf{\Phi}_{rt})\|_F^2 \tag{5}$$

where Ω performs k-space sampling, $\mathbf{F}$ performs spatial encoding, $\mathbf{S}$ performs multichannel encoding, and $\|\cdot\|_F$ denotes the Frobenius norm.

2.3.2 Rigid motion state clustering—The last inversion time of each recovery period

(i.e., immediately before the next preparation pulse is played) is extracted from $\mathbf{X}_{rt}$, creating a subset denoted as $\mathbf{X}_s$, for motion identification and motion state clustering. In this work, we assume that all the images within the same recovery period belong to the same motion state as the last inversion time of this recovery period, although multi-contrast clustering[18] is an option when faster motion time scales are desired. All images in $\mathbf{X}_s$ have similar image contrast to minimize the effect of the image contrast variation on the subsequent motion clustering, as signals from most brain tissues are close to the FLASH steady state by the last inversion time.

$\mathbf{X}_s = [\mathbf{x}_{s,1}, \mathbf{x}_{s,2}, \ldots, \mathbf{x}_{s,N_s}] \in \mathbb{C}^{N_v \times N_s}$ is organized such that the ith column $\mathbf{x}_{s,i}$ represents the vectorized 3D image at the last inversion time of the ith recovery period, where N_v and N_s denote the number of voxels and recovery periods, respectively. A k-means clustering algorithm[29] is performed on $\mathbf{X}_s$, such that the rows of $\mathbf{X}_s$ corresponds to variables and the columns of $\mathbf{X}_s$ corresponds to observations, to identify different motion states. To select the number of motion states/clusters K_0, the algorithm is performed for $K_0 = 1, 2, \ldots, 20$, and for each K_0 we calculate the sum of Euclidean distances between each feature vector and its corresponding centroid:

$$d_{K_0} = \sum_{k_0=1}^{K_0} \sum_{\mathbf{x}_{s,i} \in C_{k_0}} \|\mathbf{x}_{s,i} - \mathbf{c}_{k_0}\|_2, i \in \{1, 2, \ldots, N_s\} \tag{6}$$

where $\mathbf{c}_{k_0}$ is the centroid of the k_0th cluster C_{k_0}. We choose the K_0 heuristically at the maximal curvature of the (K_0, d_{k_0}) plot, which bears analogy to the well-known "L-curve" method for choosing the regularization parameter for ill-posed convex optimization problems[30]. Example (K_0, d_{k_0}) plots are shown in Supporting Information Figure S2, S3 and S8.

Supporting Information Video S1 demonstrates the motion clustering process in detail. $\mathbf{X}_{rt}$ contained 2760 frames (for display purpose, only 1/5, 552 frames, were shown) with

varying image contrasts (e.g., mixed relaxometry weightings). $\mathbf{X}_s$ was taken from the last inversion time of each recovery period, creating 184 frames with similar contrasts. These 184 frames were clustered into 4 different motion states. After that, the motion bins of the 2760 frames in $\mathbf{X}_{rt}$ were directly obtained by extending the bins of the 184 frames in $\mathbf{X}_s$ with respect to each recovery period. This resulting motion bins were then used to construct the motion-dedicated dimension so that indices along this dimension represented the individual motion states that occurred throughout the scan. Therefore, the motion-related variance of the data was accounted for by this motion-dedicated time dimension.

2.3.3 Multidimensional tensor subspace estimation

—In this stage, we estimate the temporal factor matrices $\mathbf{Z}$ and $\{\mathbf{V}_i\}_{i=1}^{N}$, as well as the unfolded core tensor $\mathbf{C}_{(1)}$. Together, they form the multidimensional temporal factor matrix $\mathbf{\Phi}$ according to Eq. (4).

First, without loss of generality, we denote $\mathbf{V}_1$ as the temporal basis functions for the T1 relaxation dimension. Because T1 relaxation is physically governed by the Bloch equations, $\mathbf{V}_1$ can be pre-determined from a training dictionary of feasible FLASH signal curves constructed using varying tissue and imaging parameters (TR, T1, flip angle, etc.)[18,21,22]. The SVD of this dictionary yields the factor matrix $\mathbf{V}_1$.

Second, the training data matrix $\mathbf{D}_{tr} \in \mathbb{C}^{(N_x \times N_c) \times N_t}$ stacks all the training lines in the elapsed time order (N_x, N_c, N_t represent the readout matrix size, the number of coils, and the number of training lines respectively). These training lines can be rearranged by mapping the elapsed time indices to the multidimensional time indices (i.e., inversion time, preparation index, the identified motion states), suggesting a small-scale auxiliary training tensor $\mathscr{A}_{tr}$ in the ($\mathbf{k}$, t_1, t_2, …, t_N, s)-space, i.e., $\mathscr{A}_{tr} \in \mathbb{C}^{(N_x N_c) \times N_{t_1} \times N_{t_2} \times … \times N_{t_N} \times K_0}$, where N_{t_1}, N_{t_2}, … represent the size of each time dimension. However, $\mathscr{A}_{tr}$ is likely to be incomplete and contain missing entries (i.e., zero elements), as not all contrast/motion combinations are experienced throughout the entire scan. We propose to complete the undersampled $\mathscr{A}_{tr}$ (i.e., fill the missing entries) via a Bloch-constrained small-scale LRT completion problem[18,21,22]:

$$\widehat{\mathscr{A}}_{tr} = \arg\min_{\mathbf{A}_{tr,(2)} \in \text{range}(\mathbf{V}_1)} \|[\mathbf{D}_{tr} - M(\mathscr{A}_{tr})]\mathbf{W}_r\|_F^2 + \lambda \sum_{i \neq 2} \|\mathbf{A}_{tr,(i)}\|_* + R(\mathscr{A}_{tr}) \tag{7}$$

where $M(\cdot)$ is the sampling mask applying to $\mathscr{A}_{tr}$ that preserves its non-missing entries (i.e., those entries corresponding to the t_i/s combinations that are actually experienced in $\mathbf{D}_{tr}$)[18,21,22], $\mathbf{A}_{tr,(i)}$ is the mode-i unfolding of $\mathscr{A}_{tr}$, $\|\cdot\|_*$ denotes the nuclear norm, λ weights the nuclear norm penalties, and $R(\cdot)$ applies regularization such as total variation (TV) along the motion-state dimension. $\mathbf{A}_{tr,(2)} \in \text{range}(\mathbf{V}_1)$ enforces that the T1 relaxation temporal subspace is spanned by the predetermined $\mathbf{V}_1$, where the second dimension of $\mathscr{A}_{tr}$ represents T1 relaxation[18,21,22]. $\mathbf{W}_r$ is a diagonal weighting matrix that reweights each auxiliary k-space line to reduce the effect of misidentified or outlier motion. Here $\mathbf{W}_r$ is calculated from the real-time auxiliary data residual $\mathbf{R}$:

$$\mathbf{R} = \mathbf{D}_{\text{tr}} - \mathbf{D}_{\text{tr}}\mathbf{\Phi}_{\text{tr}}^{\dagger}\mathbf{\Phi}_{\text{rt}} \tag{8}$$

and

$$W_{r,jj} = (\sum_{i=1}^{N_x \times N_c} |R_{ij}|^2)^{-1/2} \tag{9}$$

The unfolded core tensor $\mathbf{C}_{(1)}$ and the remaining temporal factor matrices can be quickly extracted from the completed $\widehat{\mathscr{A}}_{\text{tr}}$ via high-order SVD[31]. Specifically, $\{\mathbf{V}_i\}_{i=1}^{N}$ and $\mathbf{Z}$ can directly be found as the $\{L_i\}_{i=1}^{N}$ and K most significant left singular vectors of $\{\mathbf{A}_{\text{tr},(i)}\}_{i=2}^{N+2}$, while $\mathbf{C}_{(1)}$ is found as the J most significant right singular vectors of $\mathbf{A}_{\text{tr},(1)} \cdot (\mathbf{V}_1 \otimes \mathbf{V}_2 \otimes \ldots \otimes \mathbf{V}_N \otimes \mathbf{Z})$.

2.3.4 Spatial factor estimation—The final stage estimates the spatial factor matrix $\mathbf{U}$ by fitting the multidimensional temporal factor matrix $\mathbf{\Phi}$ to the imaging data, with a similar motion-weighting scheme:

$$\widehat{\mathbf{U}} = \arg\min_{\mathbf{U}} \|[\mathbf{D}_{\text{img}} - \Omega(\mathbf{FSU\Phi})]\mathbf{W}_t\|_F^2 + R_s(\mathbf{U}) \tag{10}$$

where $R_s(\cdot)$ applies spatial regularization that leverages compressed sensing. $\mathbf{W}_t$ plays a similar role to $\mathbf{W}_r$ to also tackle the misidentified or outlier motion, but reweights each individual imaging readout rather than each training readout. $\mathbf{W}_t$ is derived using Eqs. (7-8), but replacing the real-time temporal factor $\mathbf{\Phi}_{\text{rt}}$ with the multidimensional temporal factor $\mathbf{\Phi}$ with columns reordered to match the timings of $\mathbf{D}_{\text{img}}$.

The final image tensor can be reconstructed as $\widehat{\mathbf{X}}_{(1)} = \widehat{\mathbf{U}}\mathbf{\Phi}$. Figure 2 provides a graphical demonstration of the multidimensional image tensor with the application of motion-resolved T1, T2, and T1ρ mapping. There are four time dimensions in this tensor representing T1 relaxation, T2 relaxation, T1ρ relaxation, and motion-states.

2.4. Motion simulation

One set of 3D whole-brain PD/T1/T2/T1ρ maps[22] was used to generate a numerical phantom for motion simulation. K-space data corresponding to a 15min Multitasking scan were simulated, containing 96000 k-space lines in total, which followed our T1/T2/T1ρ mapping sequence[22]. Four T2-prepared inversion recovery (T2-IR) preparations with different durations (τ=[14,36,60,80]ms) and four T1ρ-prepared inversion recovery (T1ρ-IR) preparations with different spin-lock times (τ_{SL}=[15,41,65,91]ms) were cycled 50 times throughout the scan, creating 50x8=400 recovery periods (i.e., $\mathbf{X}_s$ contains 400 image frames) where each one contained N_{seg}=240 lines. A fixed sampling pattern was pre-generated according to Section 2.2, which was subsequently used for all simulation scenarios: specifically, $\mathbf{D}_{\text{tr}}$ was periodically sampled at the center k-space location (i.e., $\mathbf{k}_y=\mathbf{k}_z$=0) every 8 samples; and the rest of the data formed $\mathbf{D}_{\text{img}}$, which was sampled following Gaussian variable density along $\mathbf{k}_y$ and $\mathbf{k}_z$. The simulation pipeline is as follows:

For each time point, i.e., t from 1 to 96000:

1. Determine the preparation index

   $n_{prep} = \left\lfloor \left(t - \left(N_{\text{seg}} \times 8 \right) \times \left(\left\lceil \frac{t}{N_{\text{seg}} \times 8} \right\rceil - 1 \right) \right) / N_{\text{seg}} \right\rfloor$, and the readout index $n = t -$ $\lfloor (t-1)/N_{\text{seg}} \rfloor \times N_{\text{seg}}$, where $\lfloor \cdot \rfloor$ and $\lceil \cdot \rceil$ denotes the flooring and ceiling operators. n_{prep} ranges from 1 to 8 and determines which τ or τ_{SL} to use for the current t. n ranges from 1 to N_{seg} and determines the current inversion time.

2. Convert the 3D PD/T1/T2/T1ρ maps to a 3D multi-contrast image voxel-by-voxel, following the signal equation[22]:

$$S_t = \text{PD} \cdot \frac{1 - e^{-\frac{TR}{T1}}}{1 - e^{-\frac{TR}{T1}}\cos(\alpha)} [1 + \left(Be^{-\frac{\tau(n_{prep})}{T2}} e^{-\frac{\tau_{\text{SL}}(n_{prep})}{T1\rho}} - 1 \right) \left(e^{-\frac{TR}{T1}}\cos(\alpha) \right)^n]\sin(\alpha) \quad (11)$$

   where α denotes the FLASH flip angle, and B represents the effective inversion efficiency independent of T2 and T1ρ. Both α and B are fitted parameters and come with our numerical phantom maps.

3. Add motion to the 3D multi-contrast image depending on the current simulated motion scenario (which will be described in detail later).

4. Convert the 3D multi-contrast motion image to a 4D multi-contrast, multi-channel motion image by the multiplication of actual sensitivity maps originally calculated during the original reconstruction of the numerical phantom source images.

5. Perform 3D spatial Fourier transform on the 4D image to generate 4D k-space.

6. Add Gaussian white noise to the real and imaginary parts of the k-space data, yielding SNR≈30 (similar to the original Multitasking images used to generate the numerical phantom).

7. Take a single multi-channel k-space line from the 4D k-space at each time point according to the prescribed sampling pattern.

We evaluated the proposed motion-resolved technique under 14 motion scenarios including discrete motion and periodic motion patterns with different combinations of translational and rotational displacements. For each scenario, the corresponding k-space data was simulated according to the above pipeline. These 14 scenarios are described in detail in Supporting Information. Here we specifically highlight two scenarios that are generalizable to frequently occurred head motion patterns (as a notation, in the following text, we use (T_x, T_y, T_z) to represent the 3 translational parameters with unit millimeter, and (R_x, R_y, R_z) to represent 3 rotational parameters with unit degree):

Mixed discrete/periodic motion with regular motion scale (scenario #10, representing abrupt switch of head position and periodic nodding and/or shaking[32]): the entire 15min scan was equally divided into 5 periods (3min each). The

1st, 3rd, and 5th periods each contained a distinct motion state, where for each motion state, (T_x, T_y, T_z) and (R_x, R_y, R_z) were randomly selected from [−8mm,8mm] and [−8°,8°] – which are regular motion scales according to the literature[2,3,14,32]. The 2nd and 4th periods each contained one periodic motion, where R_z linearly transited from −8° to 8° back and forth.

Pseudo-continuous non-periodic motion with small motion scale (scenario #13, representing involuntary motion caused by breathing and/or feet wiggling[2,32,33]): the 15min simulated scan was divided into 25 periods (0.6min each). A rotation range of [0°,3°] was divided into 25 intervals to produce small rotational motion scale. The i-th period was assigned with $R_z = {}^{3i}/{}_{25}$ (deg), and the rest of the motion parameters (i.e., T_x, T_y, T_z and R_x, R_y) were set as 0. This agreed with the literature in terms of small-scale involuntary motion[2,32,33].

A comprehensive description of the 14 simulation scenarios are summarized in the online Supporting Information. The evolution of 6 motion parameters for each scenarios is shown in Supporting Information Figure S1. The simulated k-space data were used for image reconstruction. For each scenario, we went through the estimation of K_0 and the motion state clustering process without incorporating any knowledge of the ground truth motion.

2.5. In vivo experiments

Four healthy volunteers (2 females, age 36.3±16.0 years) were scanned on a 3T clinical scanner (Biograph mMR, Siemens Healthineers, Erlangen, Germany) using a 20-channel head coil. The study was approved by the institutional review board of our institution. Our T1/T2/T1ρ mapping sequence was implemented[22]. Scan parameters were: FOV=240x240x140mm^3, voxel size=1.0x1.0x3.5mm^3, FLASH TR/TE=9.4/4.9ms, FLASH flip angle=5°. Four T2-IR and four T1ρ-IR preparations were cycled 23 times throughout the scan, leading to a scan time of 7min with 23x8=184 recovery periods (i.e., $\mathbf{X}_s$ contains 184 image frames). The data sampling employed 1 training line ($\mathbf{D}_{tr}$) collected at the center k-space followed by 15 imaging lines ($\mathbf{D}_{img}$) collected with Gaussian variable density along $\mathbf{k}_y$ and $\mathbf{k}_z$.

The Multitasking sequence was performed three times for each subject. A 3.5s low-resolution calibration scan preceded each Multitasking scan for sensitivity map estimation using ESPIRiT[34]. For the first scan, the subject was instructed to remain still, generating a motion-free scenario as a reference. For the second scan, the subject was instructed to perform discrete motion more than twice during the 7min. The subject was allowed to decide for themselves at which point during the 7min they would move, how many times they would move, which direction they would move each time, and the amount of displacement. For the third scan, the subject was instructed to perform periodic motion for at least 2min during the 7min. The subject was allowed to decide for themselves at what point during the 7min they would start moving, how long they would move, whether they performed periodic shaking or nodding, and the amount of displacement. Subjects were not instructed to return to the original position after the movement, allowing scenarios such as discrete plus periodic motion. The subjects were given as much freedom in terms of the

motion as possible, in order to mimic a real clinical scenario and to rule out any prior knowledge about the specific motions each subject would perform. The volunteers were instructed on the two types of motion before entering the scan room.

2.6. Evaluation

Image reconstructions were performed on a Linux workstation with a 2.70GHz dual 12-core Intel Xeon processor equipped with 256GB RAM and running MATLAB 2016b (MathWorks, Natick, Massachusetts). The motion simulation time (i.e., steps 1–7 in section 2.4) was ~6.1h per simulation scenario regardless of the motion pattern. The image reconstruction time was ~1.6h per dataset (both for simulated data and in vivo data) regardless of the motion pattern. The ranks of different parameter dimensions were chosen as $L_1=5$, $L_2=4$, and $L_3=4$, respectively, the rank of the motion dimension $K = K_0$, and the rank of the spatial dimension J was chosen between 5 to 20, depending on the motion patterns. It is expected that more complicated motion patterns would lead to higher J. T1/T2/T1ρ maps were obtained from the reconstructed image tensor $\widehat{\mathbf{X}}_{(1)}$ following Eq. (11) using the MATLAB nonlinear least-squares solver (lsqnonlin) based on the trust-region-reflective algorithm[35].

For both simulation and in vivo experiments, three motion-handling reconstructions were performed on each dataset: i) no motion handling, where all k-space data were assigned to a single motion state (i.e., $K_0=1$); ii) motion-removal, where only the k-space data belonging to the most populous motion bin were used for reconstruction, and the rest of the k-space data were discarded; iii) motion-resolved, as described in Section 2.2. The T1/T2/T1ρ maps were obtained for each reconstruction.

For simulation experiments, the numerical phantom itself was used as the reference images for subsequent comparisons. Root-mean-squared-error (RMSE) and structural similarity index measure (SSIM) of the reconstructed T1/T2/T1ρ maps against the reference images were calculated for each reconstruction in each simulated scenario. The motion state corresponding to the same spatial position as the reference images were used for T1/T2/T1ρ fitting.

For in vivo experiments, the most populous motion state was used for T1/T2/T1ρ fitting (i.e., might be misaligned from the reference). For each subject, an axial slice around the middle portion of the brain where the ventricle could be clearly seen while the putamen was still invisible was chosen for ROI analysis. White matter (WM) and cortical gray matter (GM) ROIs were obtained by thresholding the reconstructed image tensor at a fixed inversion time (1219ms) along the T1 time dimension[22]. Quantitative WM/GM T1/T2/T1ρ measurements were calculated and compared with the motion-free reference for each reconstruction in each subject.

3. Results

3.1. Simulation results

Mixed discrete/periodic motion with regular motion scale: Supporting Information Figure S2 shows the "L-curve"-like (K_0, d_{K_0}) plot, where $K_0=7$ was chosen at the maximum

curvature, and the associated binning of 7 motion states. Figure 3 shows the comparison of the three motion-handling reconstruction methods. Substantial blurring and almost complete loss of image features were observed if no motion handling was done, with exceptionally large absolute difference errors in T1/T2/T1ρ against the reference maps. With motion-removal, most artifacts disappeared and image features were recovered. The proposed motion-resolved solution not only improved the image quality, but also further reduced the absolute difference errors in T1/T2/T1ρ compared to motion-removal. Supporting Information Video S2 shows the example $\mathbf{X}_s$ images and the identified 7 motion states.

Pseudo-continuous non-periodic motion with small motion scale: Supporting Information Figure S3 shows the "L-curve"-like (K_0, d_{K_0}) plot and the motion state binning results. $K_0=5$ was chosen at the maximum curvature rather than the ground truth $K_0=25$. The clustered 5 motion states were approximately equal in duration. Figure 4 shows the comparison of the three motion-handling reconstruction methods. For small-scale displacements, without motion handling, the blurring artifacts could still be observed especially in GM/WM boundaries, leading to the highest absolute difference errors in T1/T2/T1ρ maps. Both motion-removal and motion-resolved approaches produced T1/T2/T1ρ maps with sharp tissue structures and good image quality, while the motion-resolved solution yielded notably less absolute difference errors than simple motion-removal. Supporting Information Video S3 shows the example $\mathbf{X}_s$ images and the identified 5 motion states.

Aside from the two representative motion scenarios, other simulation scenarios were also investigated (Supporting Information Figures S4-S9; Supporting Information Videos S4-S8). The motion-resolved method demonstrated superior performance over motion-removal and no motion handling, producing the best reconstructed T1/T2/T1ρ image quality free from motion-induced ghosting artifacts and the least absolute difference errors against the reference maps, under all simulation scenarios with various combinations of translation and rotation.

RMSE and SSIM of the reconstructed T1/T2/T1ρ against the reference images for all 14 simulation scenarios were shown in Figure 5. For motion-resolved, motion-removal, and no motion handling respectively, RMSE and SSIM of T1 were (17.20±7.27ms, 46.10±18.23ms, 168.40±72.89ms) and (0.9758±0.0190, 0.9301±0.0381, 0.7565±0.0869); RMSE and SSIM of T2 were (1.47±0.46ms, 2.77±0.66ms, 9.73±5.23ms) and (0.9476±0.0269, 0.9069±0.0332, 0.7148±0.0916); RMSE and SSIM of T1ρ were (1.57±0.48ms, 2.88±0.76ms, 11.06±6.96ms) and (0.9492±0.0264, 0.9087±0.0339, 0.7074±0.0945).

3.2. In vivo results

Supporting Information Figure S10 shows the results under moderate discrete motion (as likely to occur in real clinical cases) from one subject. Corresponding $\mathbf{X}_s$ images and the identified $K_0=3$ motion states are shown in Supporting Information Video S9. The proposed method restored T1/T2/T1ρ maps resembling the motion-free reference, while apparent blurring and ghosting artifacts were observed without motion handling. Motion-removal produced biased parameter maps and loss of image features.

Figure 6 shows the results under large discrete motion (less likely to occur in real clinical cases) from one subject. Corresponding $\mathbf{X}_s$ images and the identified $K_0=4$ motion states are shown in Supporting Information Video S10. Despite the notably large translation and rotation in this scenario, motion-resolved T1/T2/T1ρ maps were recovered with good image quality. Motion-removal produced substantially biased parameter maps and loss of image features, while notable motion artifacts were seen without motion handling.

One volunteer performed "tremor-like" head motion during their discrete motion session. More than 15 movements were performed in 7min, which were clustered into $K_0=6$ motion bins shown in Supporting Information Video S11 along with the $\mathbf{X}_s$ images. This case resembled patient movement with Parkinson's disease or epilepsy. Motion-resolved T1/T2/T1ρ maps were with good image quality and sharp tissue structures. Ghosting artifacts were seen without motion handling. Motion-removal led to blurring and substantial loss of image features. (Figure 7).

Supporting Information Video S12 and S13 demonstrate two periodic motion scenarios on two subjects and the respective motion state clustering results – S12 corresponds to periodic shaking ($K_0=4$) and S13 corresponds to periodic nodding ($K_0=4$). For both cases, the proposed method was effective in recovering T1/T2/T1ρ maps with the best image quality, consistent with the performance as in discrete motion scenarios (Figure 8; Figure 9).

Figure 10 shows the quantitative T1/T2/T1ρ measurements of WM and GM of all four subjects. On average across all subjects (considering both motion types), no motion handling, motion-removal, and motion-resolved produced: 7.0%, 6.0%, 0.6% absolute difference against the reference T1 mean, and 186.6% higher, 71.8% higher, 4.7% lower than the reference T1 standard deviation; 7.8%, 7.0%, 1.0% absolute difference against the reference T2 mean, and 292.6% higher, 80.1% higher, 8.8% higher than the reference T2 standard deviation; 4.9%, 6.9%, 0.9% absolute difference against the reference T1ρ mean, and 253.6% higher, 94.4% higher, 1.5% higher than the reference T1ρ standard deviation.

4. Discussion

We proposed a motion-resolved solution to quantitative multiparametric brain MRI using the Multitasking framework. This framework conceptualizes overlapping image dynamics as different time dimensions. An LRT image model is used to simultaneously resolve motion and other tissue parameters by exploiting the spatiotemporal correlation of the multidimensional image function. Motion simulations were performed for various scenarios including discrete motion and periodic motion that involved different combinations of translation and rotation, as well as a total-displacement exploration over both large and small translations and rotations. In vivo experiments were conducted to investigate the performance under discrete and periodic motion. The proposed method handled both cases well by producing parametric maps with good image quality free from motion artifacts and quantitative measurements closely resembling the motion-free reference measurements.

Popular techniques to address brain motion include motion tracking using either external hardware[2,3] or navigator/image signals[4-6], prospective and retrospective motion

correction[4,7-9]. The proposed method does not rely on external motion-monitoring devices, which simplifies the scanning workflow. The head motion patterns throughout the scan were identified and binned into different motion states via unsupervised clustering. The dynamic head motion process was then captured with one motion-dedicated time dimension and motion-resolved imaging was achieved by modeling the signal correlation between different motion states along this dimension, so that there was no explicit need for image registration-based motion correction between these motion states to account for deformation, translation, and rotation. Note that motion correction between different motion states could be complementary to the current framework by registering all motion states to a target state, which could have the benefit of improving signal correlation along motion dimension, thus further facilitating low-rankness and reducing the degrees of freedom[20]. However, because head motion is a composition of translation and rotation, motion correction with rigid-body transform would lead to non-Cartesian k-space not inherently compatible with Cartesian FFT reconstruction. Future works may investigate stack-of-stars or stack-of-spiral trajectories that provide better motion robustness and are more straightforward for rotational motion correction.

Other self-gated multidimensional techniques such as XD-GRASP[17] have been recently demonstrated in the heart and abdomen, and may also be useful in the brain if similarly adapted. XD-GRASP was not originally described for relaxometry, and its use of first-order finite difference sparsity (temporal total variation) could induce physically unrealistic piece-wise steps in the relaxation dimensions; however, expansion of the XD-GRASP approach to induce high-order finite differences could be appropriate for the smooth temporal curves associated with relaxation. Even so, Multitasking has potential practical advantages over XD-GRASP and similar approaches. Multitasking reconstructs images in compressed form, as individual factors are recovered, and all calculations are done in low-dimensional subspaces. This is in contrast to compressed sensing approaches like XD-GRASP which recover images that are "compressible" but not actually compressed. This memory advantage is a major practical consideration when there are many timepoints to recover, as in high-dimensional problems. For example, with $J=5$ and $K=4$, the total memory of Multitasking factors $\mathbf{U}$, $\mathbf{V}_1$, $\mathbf{V}_2$, $\mathbf{V}_3$, $\mathbf{Z}$ and $\mathscr{C}$ was 16B/entry $\times$ ($N_x N_y N_z J$ + $N_{T1} L_1 + N_{T2} L_2 + N_{T1\rho} \times L_3 + K_0 K + JKL_1 L_2 L_3$)entries = 176 MB at complex double precision. If the entire image tensor was instead stored and operated upon, it would require 16B/entry $\times$ ($N_x N_y N_z N_{T1} N_{T2} N_{T1\rho} K_0$)entries = 527 GB. Generally speaking, the factorized LRT approach would offer a memory/storage advantage whenever $N_x N_y N_z J + \sum_{i=1}^{N} N_{t_i} L_i + K_0 K + JK \prod_{i=1}^{N} L_i < N_x N_y N_z K_0 \prod_{i=1}^{N} N_{t_i}$.

There are several different ways of considering motion within the Multitasking framework. It is possible to ignore motion, as if all the data belong to a single motion state (i.e., $K_0=1$). However, when motion does exist, this assumption would cause spatiotemporal blurring by grouping data of different spatial positions into the same bin during temporal subspace estimation. Therefore, the reconstructed images would be corrupted by motion. A separate strategy is motion-removal, which was adopted in our brain T1/T2/ADC and T1/T2/T1ρ mapping techniques[21,22], where the corrupted data were identified either by visual inspection or through real-time auxiliary data residual and subsequently removed

to avoid introducing motion artifacts. This solution may suffice when only a brief portion of the acquisition is corrupted by motion (i.e., suddenly switching position and quickly returning to the initial position). However, in real cases, patients do not necessarily return to the initial position. Therefore, motion-removal can result in a significant loss of information and heavy undersampling artifacts when only very few data are kept, leading to subpar reconstruction and corrupted quantitative measurements in extreme scenarios. The motion-resolved reconstruction detailed here exploits multidimensional signal correlation and retains all the data for reconstruction, which is data-efficient, greatly improves the image quality, and can be applied to a wide variety of motion types. We have demonstrated the effectiveness of motion-resolved imaging in the brain: for simulations, the motion-resolved solution yielded smaller RMSE and higher SSIM, and for in vivo experiments, the motion-resolved solution produced T1/T2/T1ρ maps with much more improved image quality and similar measurement distributions to the motion-free reference.

The proposed method provides a unified motion-resolved framework that is generalizable to discrete and periodic motion patterns that compose translation and rotation. These motion patterns have been widely studied and frequently occur during head shaking and head nodding in clinical brain MRI[32]. The effectiveness of the proposed method has been demonstrated under reasonable ranges of translational distances (−8mm–8mm) and rotational angles (−8°–8°) which has been reported in previous studies[2,3,14,32], as well as exceptionally large translational distances (up to 60mm) and rotational angles (up to 60°) that are less likely to occur in clinical MRI. Very small translation and rotation (usually within 1mm and 1°) could also happen in clinical MRI in the form of involuntary motion induced by breathing or feet wiggling[2,32,33]. In simulation scenarios #13 and #14, our motion detection and clustering algorithms identified 5 motion states out of the ground truth 25 motion states linearly spaced between 0–3mm and 0–3° respectively, indicating the smallest detectable motion ranges within 0.6mm and 0.6°. Motion states that are separated by <0.6mm or <0.6° could be binned together without introducing notable blurring under the acquired voxel size of 1x1x3.5mm^3. However, for ultra-high spatial resolution (0.5mm), involuntary motion may create spatial blurring between voxels necessitating a higher number of motion states.

In this work, only $\mathbf{X}_s$ corresponding to the last inversion time of each recovery period in $\mathbf{X}_{rt}$ were used for motion identification. Images in $\mathbf{X}_s$ have very similar image contrasts as shown in all supporting videos, as every image in $\mathbf{X}_s$ is the closest to the FLASH steady state of the corresponding recovery period. This minimizes the effect of the varying image contrast throughout the scan on the subsequent motion clustering. The use of $\mathbf{X}_s$ for motion identification is based on the assumption that all the data belong to the same motion state in each recovery period, which can be represented by the motion state at the last inversion time. This assumption is valid if the time scale for motion is longer than TR (~2.3s in our study) so that a single motion state is contained in one TR, usually when motion happens at random and at low frequency. If the time scale for motion is shorter than TR and more than one motion states occur during a single TR, which is usually the case of periodic motion or the transition periods between different motion states, they are considered as misidentified or outlier motion and are properly weighted by the motion weighting matrices.

A similar strategy has been applied to our abdominal DCE study[20]. Note that it is possible to incorporate the multi-contrast model into the motion clustering algorithm to handle the dynamically varying image contrasts, which allows motion states to be resolved at motion time scales shorter than TR (for example, in the heart)[18].

It is worth mentioning that although this work focused on motion-resolved T1/T2/T1ρ mapping as an application, the proposed method could be extended to other tissue parameter combinations that are available with the Multitasking framework, including but not limited to T1/T2/ADC[21], T1/T2/T1ρ/T2*/QSM[36], T1/T2*/proton density fat fraction (PDFF)[37], CEST[38], and perfusion and vascular permeability parameters with DCE MRI[20,23,24], with proper sequence modification but without changing the reconstruction pipeline. We aim to provide a unified framework generalizable enough to not only different head motion patterns, but also different tissue parameters in various clinical applications. More investigation on other tissue parameters in the brain as well as clinical studies will be conducted in the future.

5. Conclusion

We proposed a motion-resolved solution for quantitative multiparametric brain MRI using MR Multitasking. For simultaneous T1/T2/T1ρ mapping, motion-resolved imaging heavily reduced motion artifacts and provided comparable quantitative measurements to motion-free references, which greatly outperformed motion-removal or no motion handling. The extension to other tissue parameter combinations is straightforward within the proposed framework. The motion-resolved solution is generalizable to translation, rotation, discrete motion, and periodic motion without requiring external motion-tracking devices or explicit need for registration-based motion compensation, providing a potential avenue for efficiently addressing head motion in quantitative brain MRI for clinical applications.

Supplementary Material

Refer to Web version on PubMed Central for supplementary material.

Acknowledgements

References

1. Andre JB, Bresnahan BW, Mossa-Basha M, Hoff MN, Smith CP, Anzai Y, et al. Toward Quantifying the Prevalence, Severity, and Cost Associated With Patient Motion During Clinical MR Examinations. J Am Coll Radiol. 2015;12(7):689–95. [PubMed: 25963225]

2. Qin L, van Gelderen P, Derbyshire JA, Jin F, Lee J, de Zwart JA, et al. Prospective head-movement correction for high-resolution MRI using an in-bore optical tracking system. Magn Reson Med. 2009;62(4):924–34. [PubMed: 19526503]

3. Ooi MB, Krueger S, Thomas WJ, Swaminathan SV, Brown TR. Prospective real-time correction for arbitrary head motion using active markers. Magn Reson Med. 2009;62(4):943–54. [PubMed: 19488989]

4. Godenschweger F, Kagebein U, Stucht D, Yarach U, Sciarra A, Yakupov R, et al. Motion correction in MRI of the brain. Phys Med Biol. 2016;61(5):R32–56. [PubMed: 26864183]

5. Pipe JG. Motion correction with PROPELLER MRI: application to head motion and free-breathing cardiac imaging. Magn Reson Med. 1999;42(5):963–9. [PubMed: 10542356]

6. Thesen S, Heid O, Mueller E, Schad LR. Prospective acquisition correction for head motion with image-based tracking for real-time fMRI. Magn Reson Med. 2000;44(3):457–65. [PubMed: 10975899]

7. Maclaren J, Herbst M, Speck O, Zaitsev M. Prospective motion correction in brain imaging: a review. Magn Reson Med. 2013;69(3):621–36. [PubMed: 22570274]

8. Bookwalter CA, Griswold MA, Duerk JL. Multiple overlapping k-space junctions for investigating translating objects (MOJITO). IEEE Trans Med Imaging. 2010;29(2):339–49. [PubMed: 19709968]

9. Vaillant G, Prieto C, Kolbitsch C, Penney G, Schaeffter T. Retrospective Rigid Motion Correction in k-Space for Segmented Radial MRI. IEEE Trans Med Imaging. 2014;33(1):1–10. [PubMed: 23782798]

10. Zaitsev M, Maclaren J, Herbst M. Motion artifacts in MRI: A complex problem with many partial solutions. J Magn Reson Imaging. 2015;42(4):887–901. [PubMed: 25630632]

11. Deoni SC, Peters TM, Rutt BK. High-resolution T1 and T2 mapping of the brain in a clinically acceptable time with DESPOT1 and DESPOT2. Magn Reson Med. 2005;53(1):237–41. [PubMed: 15690526]

12. Ma D, Gulani V, Seiberlich N, Liu K, Sunshine JL, Duerk JL, et al. Magnetic resonance fingerprinting. Nature. 2013;495(7440):187–92. [PubMed: 23486058]

13. Mehta BB, Ma D, Pierre EY, Jiang Y, Coppo S, Griswold MA. Image reconstruction algorithm for motion insensitive MR Fingerprinting (MRF): MORF. Magn Reson Med. 2018;80(6):2485–2500. [PubMed: 29732610]

14. Yu Z, Zhao T, Asslander J, Lattanzi R, Sodickson DK, Cloos MA. Exploring the sensitivity of magnetic resonance fingerprinting to motion. Magn Reson Imaging. 2018;54:241–248. [PubMed: 30193953]

15. Cao X, Ye H, Liao C, Li Q, He H, Zhong J. Fast 3D brain MR fingerprinting based on multi-axis spiral projection trajectory. Magn Reson Med. 2019;82(1):289–301. [PubMed: 30883867]

16. Kurzawski JW, Cencini M, Peretti L, Gomez PA, Schulte RF, Donatelli G, et al. Retrospective rigid motion correction of three-dimensional magnetic resonance fingerprinting of the human brain. Magn Reson Med. 2020;84(5):2606–2615. [PubMed: 32368835]

17. Feng L, Axel L, Chandarana H, Block KT, Sodickson DK, Otazo R. XD-GRASP: Golden-angle radial MRI with reconstruction of extra motion-state dimensions using compressed sensing. Magn Reson Med. 2016;75(2):775–88. [PubMed: 25809847]

18. Christodoulou AG, Shaw JL, Nguyen C, Yang Q, Xie Y, Wang N, et al. Magnetic resonance multitasking for motion-resolved quantitative cardiovascular imaging. Nat Biomed Eng. 2018;2(4):215–226. [PubMed: 30237910]

19. Shaw JL, Yang Q, Zhou Z, Deng Z, Nguyen C, Li D, et al. Free-breathing, non-ECG, continuous myocardial T1 mapping with cardiovascular magnetic resonance multitasking. Magn Reson Med. 2019;81(4):2450–2463. [PubMed: 30450749]

20. Wang N, Gaddam S, Wang L, Xie Y, Fan Z, Yang W, et al. Six-dimensional quantitative DCE MR Multitasking of the entire abdomen: Method and application to pancreatic ductal adenocarcinoma. Magn Reson Med. 2020;84(2):928–948. [PubMed: 31961967]

21. Ma S, Nguyen CT, Han F, Wang N, Deng Z, Binesh N, et al. Three-dimensional simultaneous brain T1 , T2 , and ADC mapping with MR Multitasking. Magn Reson Med. 2020;84(1):72–88. [PubMed: 31765496]

22. Ma S, Wang N, Fan Z, Kaisey M, Sicotte NL, Christodoulou AG, et al. Three-dimensional whole-brain simultaneous T1, T2, and T1rho quantification using MR Multitasking: Method and initial clinical experience in tissue characterization of multiple sclerosis. Magn Reson Med. 2021;85(4):1938–1952. [PubMed: 33107126]

23. Wang N, Christodoulou AG, Xie Y, Wang Z, Deng Z, Zhou B, et al. Quantitative 3D dynamic contrast-enhanced (DCE) MR imaging of carotid vessel wall by fast T1 mapping using Multitasking. Magn Reson Med. 2019;81(4):2302–2314. [PubMed: 30368891]

24. Wang N, Xie Y, Fan Z, Ma S, Saouaf R, Guo Y, et al. Five-dimensional quantitative low-dose Multitasking dynamic contrast- enhanced MRI: Preliminary study on breast cancer. Magn Reson Med. 2021;85(6):3096–3111. [PubMed: 33427334]

25. Christodoulou AG, Lingala SG. Accelerated Dynamic Magnetic Resonance Imaging Using Learned Representations: A New Frontier in Biomedical Imaging. IEEE Signal Proc Mag. 2020;37(1):83–93.

26. He J, Liu Q, Christodoulou A, Ma C, Lam F, Liang Z-P. Accelerated high-dimensional MR imaging with sparse sampling using low-rank tensors. IEEE Trans Med Imaging. 2016;35(9):2119–2129. [PubMed: 27093543]

27. Liang Z-P. Spatiotemporal imagingwith partially separable functions. *In* Proceedings of the 4th IEEE International Symposium on Biomedical Imaging: From Nano to Macro, Arlington, Virginia, USA, 2007. p. 988–991.

28. Tucker LR. Some mathematical notes on three-mode factor analysis. Psychometrika. 1966;31(3):279–311. [PubMed: 5221127]

29. Lloyd S Least squares quantization in PCM. IEEE Trans Inf Theory. 1982;28(2):129–137.

30. Calvetti D, Morigi S, Reichel L, Sgallari F. Tikhonov regularization and the L-curve for large discrete ill-posed problems. J Compute Appl Math. 2000;123(1-2):423–446.

31. De Lathauwer L, De Moor B, Vandewalle J. A multilinear singular value decomposition. Siam J Matrix Anal A. 2000;21(4):1253–1278.

32. Wallace TE, Afacan O, Waszak M, Kober T, Warfield SK. Head motion measurement and correction using FID navigators. Magn Reson Med. 2019;81(1):258–274. [PubMed: 30058216]

33. Bortolotti L, Mougin O, Bowtell R. Measurement of head motion using a field camera in a 7T scanner. In Proceedings of the 28th Annual Meeting of ISMRM Virtual Conference and Exhibition, 2020. p 0464.

34. Uecker M, Lai P, Murphy MJ, Virtue P, Elad M, Pauly JM, et al. ESPIRiT--an eigenvalue approach to autocalibrating parallel MRI: where SENSE meets GRAPPA. Magn Reson Med. 2014;71(3):990–1001. [PubMed: 23649942]

35. Coleman TF, Li Y. An interior trust region approach for nonlinear minimization subject to bounds. SIAM J Optim. 1996;6(2):418–445.

36. Ma S, Cao T, Wang N, Christodoulou AG, Fan Z, Xie Y, et al. 10min Whole-Brain Solution – Comprehensive Quantification of MR Relaxometry and Susceptibility Plus Synthetic Contrast-Weighted Images. *In* Proceedings of the 29th Annual Meeting of ISMRM: An Online Experience, 2021. P 0101.

37. Wang N, Cao T, Han F, Xie Y, Zhong X, Ma S, et al. Six-Dimensional, Free-Breathing Multitasking Multi-Echo (MT-ME) MRI for Whole-Liver T1, PDFF, and R2* Quantification. In Proceedings of the 29th Annual Meeting of ISMRM: An Online Experience, 2021. P 0609.

38. Han P, Cheema K, Lee H-L, Zhou Z, Cao T, Ma S, et al. Whole-Brain Steady-State CEST at 3T Using MR Multitasking. *In* Proceedings of the 29th Annual Meeting of ISMRM: An Online Experience, 2021. P 1456.
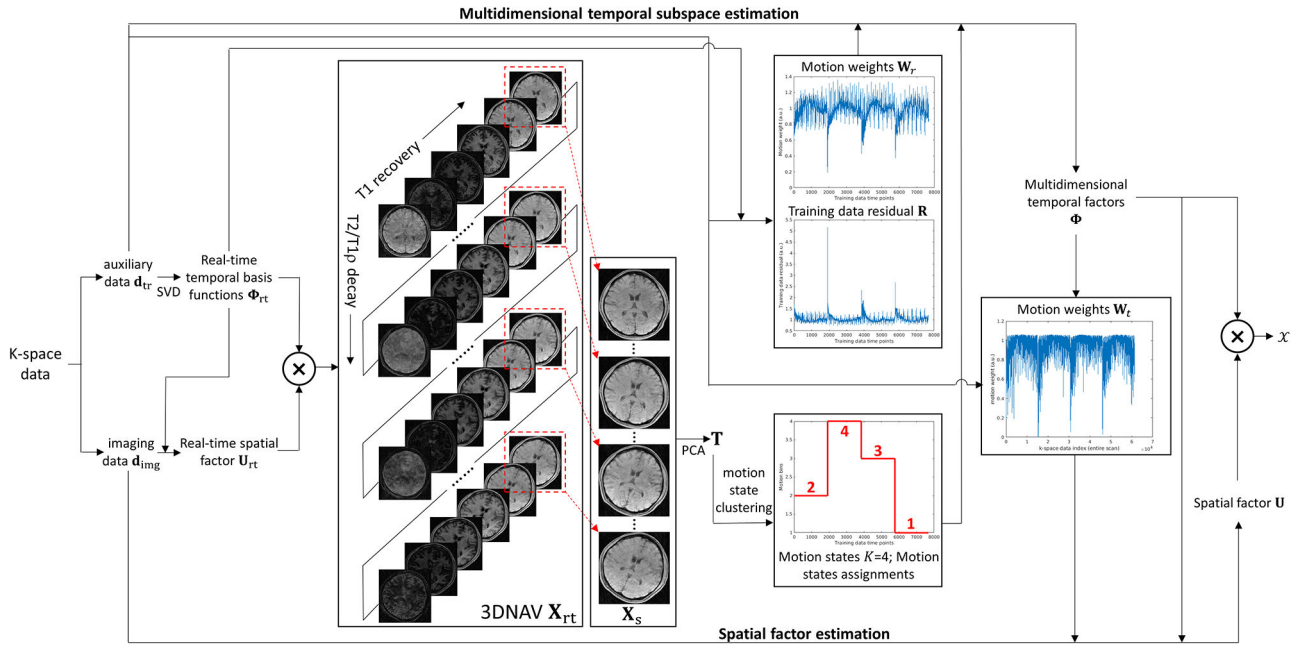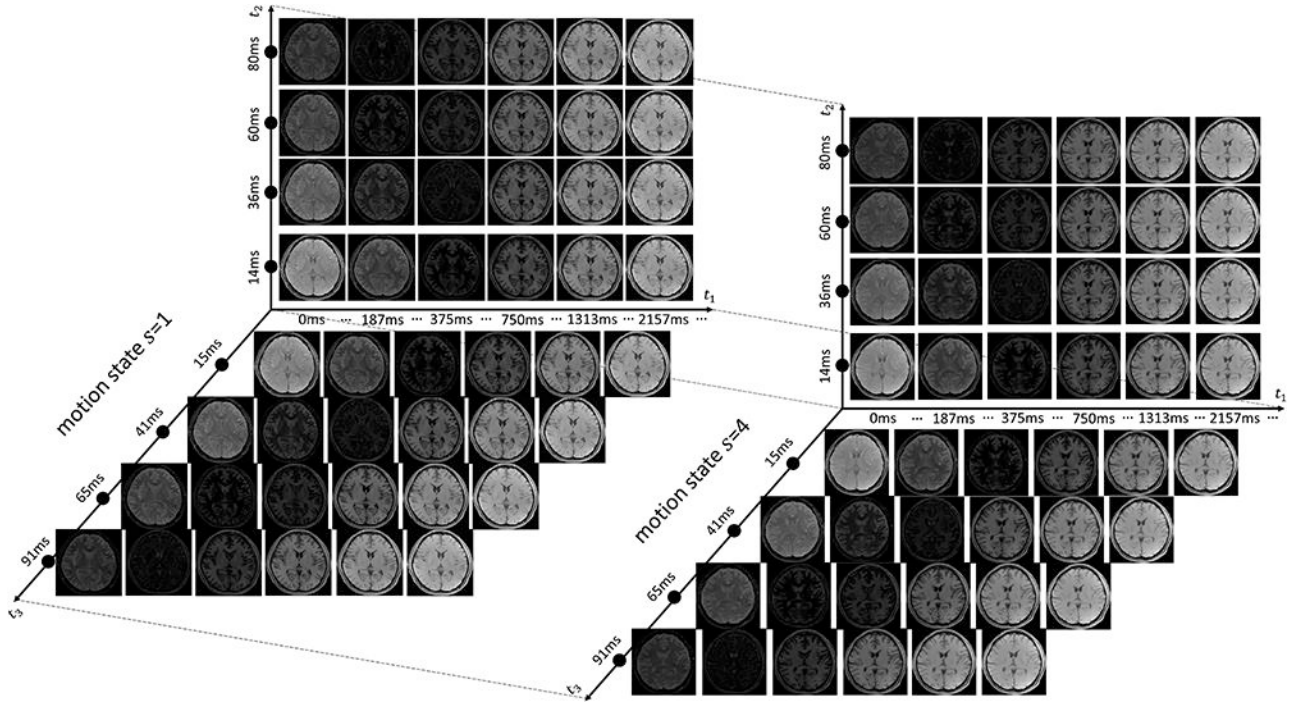
Figure 1.
Motion-resolved image reconstruction schematics. The dataset of the entire k-space lines is a union of two non-overlapping subsets: auxiliary training data (green) and imaging data (red). 3DNAV images $\mathbf{X}_{rt}$ contain a mixture of T1/T2/T1ρ contrasts and different motion states. The last inversion time of each recovery period is extracted from $\mathbf{X}_{rt}$, creating $\mathbf{X}_s$ for motion identification. Example motion weights $\mathbf{W}_r$, auxiliary training data residuals and motion state assignments are shown for tensor subspace estimation. Motion weights $\mathbf{W}_t$ are calculated from the multidimensional temporal factors. Low motion weightings reduce the effect of misidentified or outlier motion.

Figure 2.
Multidimensional image tensor demonstration with four time dimensions – T1 relaxation
dimension (t_1), T2 relaxation dimension (t_2), T1ρ relaxation dimension (t_3), and motion state
dimension (s). There are 240 inversion times along T1 relaxation dimension (6 are shown),
4 T2-IR preparation durations along T2 relaxation dimension (all are shown) , 4 T1ρ-IR
preparation durations (TSL) along T1ρ relaxation dimension (all are shown), and 4 motion
states along motion state dimension (only motion state 1 and 4 are shown).
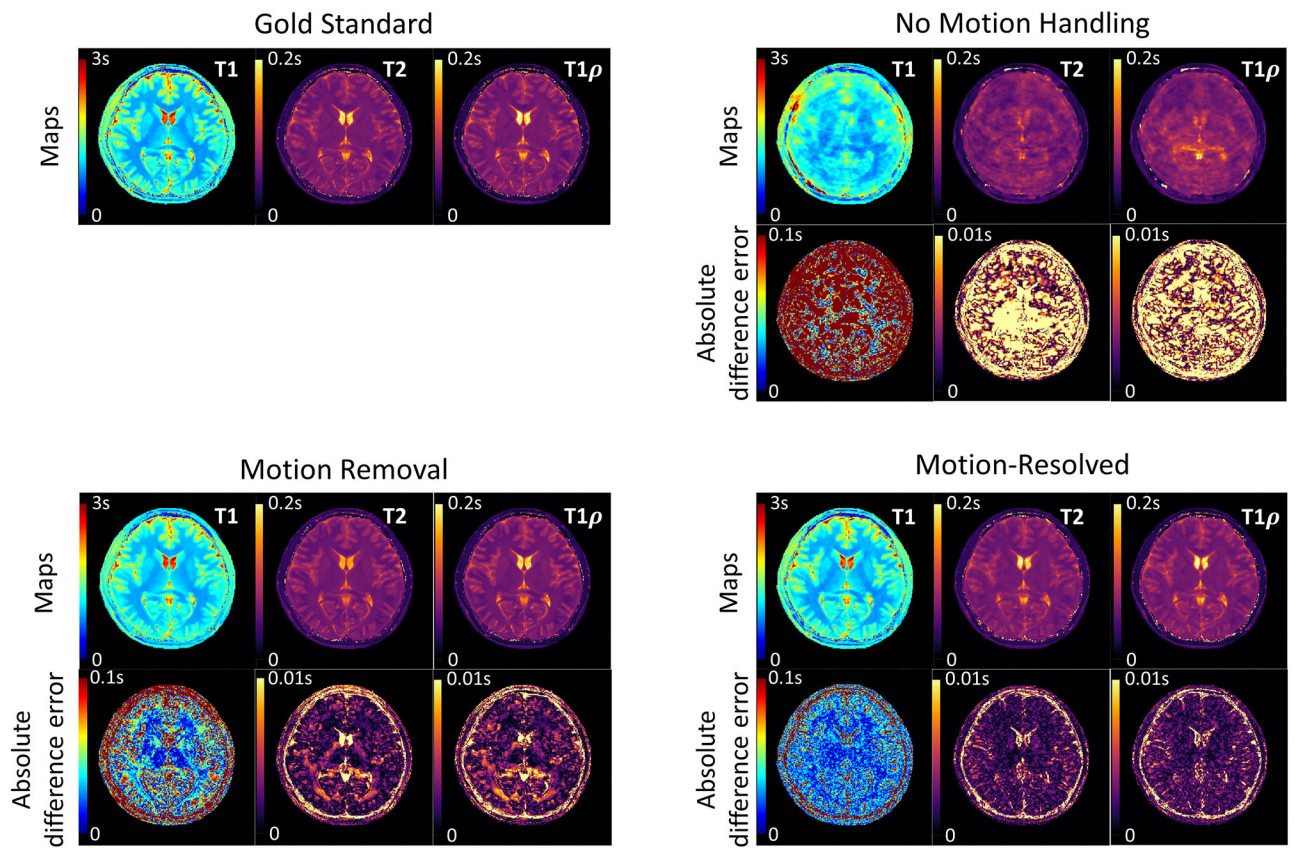
Figure 3.
Simulation results of mixed discrete/periodic motion with regular motion scale (scenario #10). The 1st motion state is used for fitting. Top left: numerical phantom T1/T2/T1ρ maps as reference images. Top right: reconstructed T1/T2/T1ρ maps and error maps against the reference images without motion handling. Bottom left: reconstructed T1/T2/T1ρ maps and error maps against the reference images with motion removal. Bottom right: motion-resolved T1/T2/T1ρ maps and error maps against the reference images.
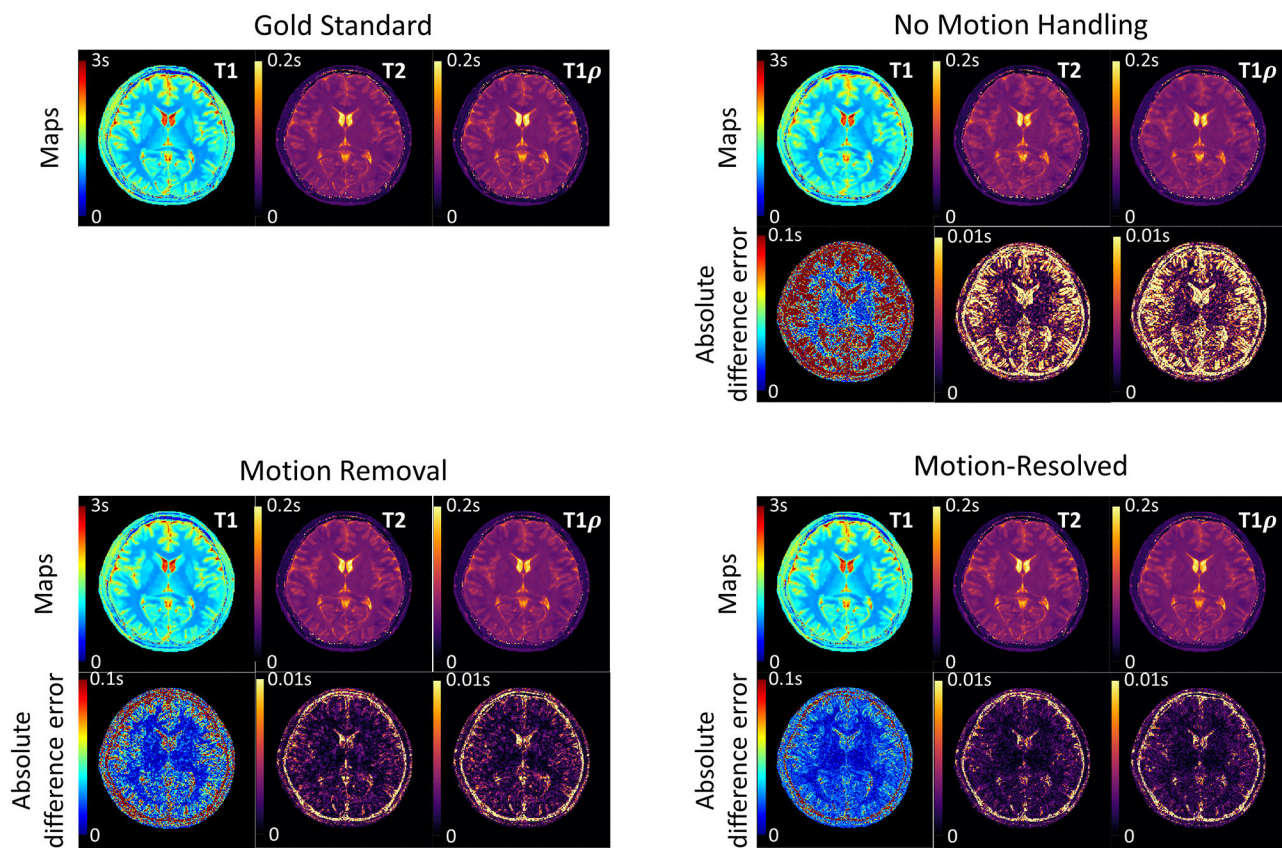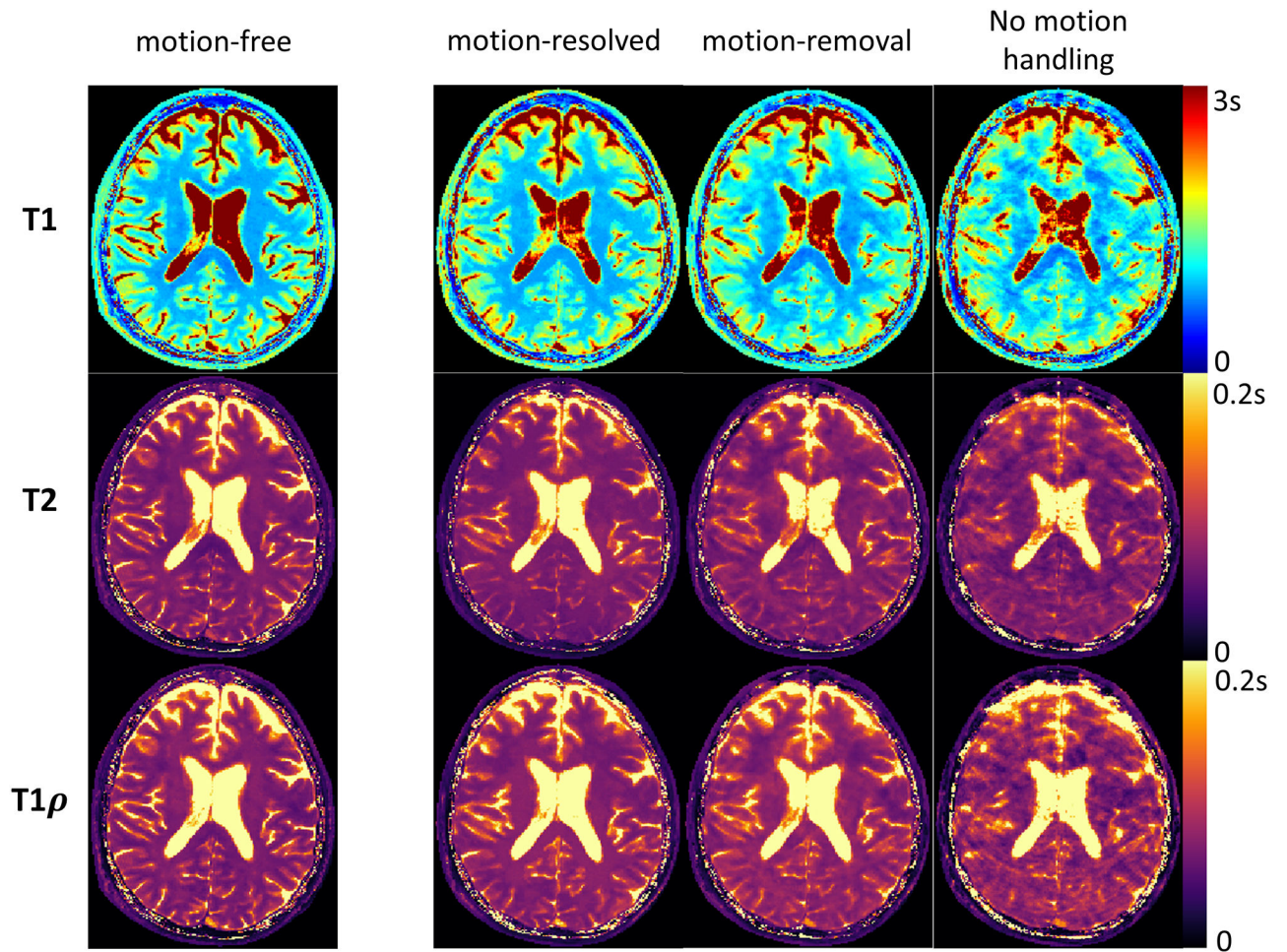
Figure 4.
Simulation of pseudo-continuous non-periodic motion with small motion scale (scenario #13). The 1st motion state is used for fitting. Top left: numerical phantom T1/T2/T1ρ maps as reference images. Top right: reconstructed T1/T2/T1ρ maps and error maps against the reference images without motion handling. Bottom left: reconstructed T1/T2/T1ρ maps and error maps against the reference images with motion removal. Bottom right: motion-resolved T1/T2/T1ρ maps and error maps against the reference images.
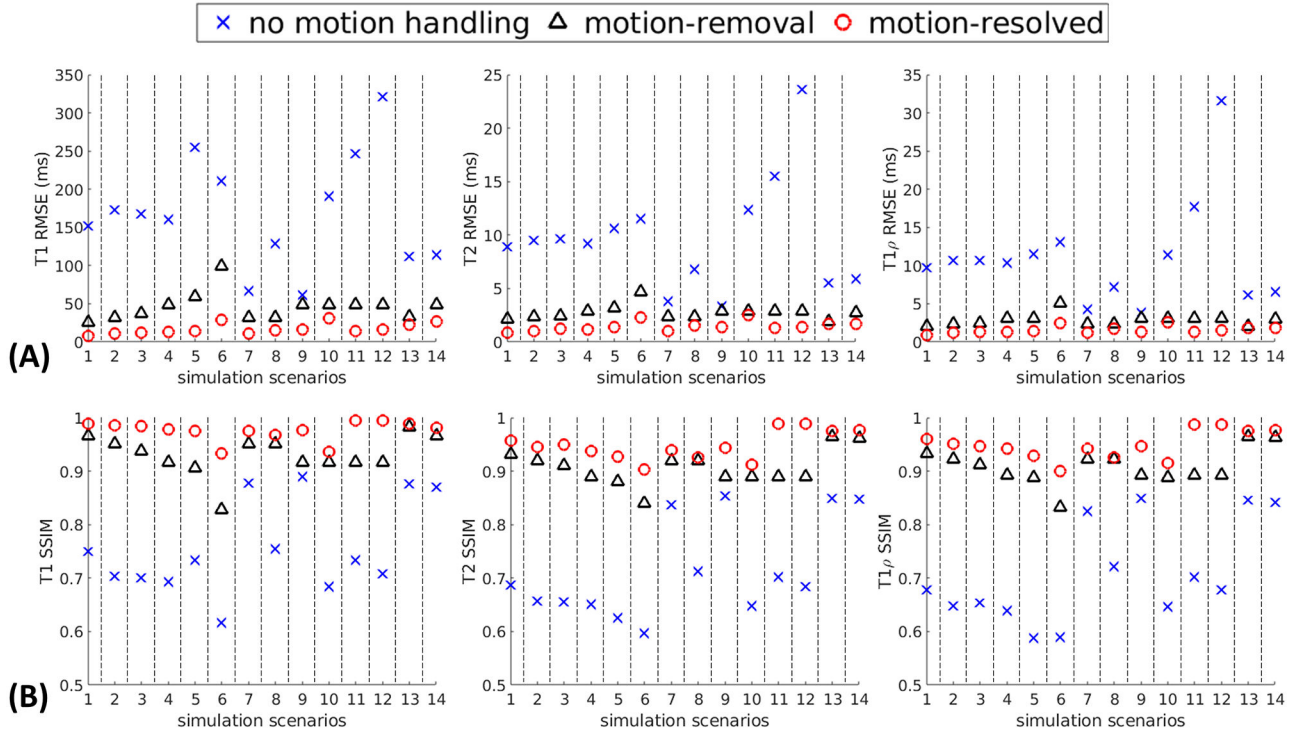
Figure 5.
(A) RMSE of T1/T2/T1ρ against the reference images for the 14 simulation scenarios. The proposed method (motion-resolved) produces the least RMSE for all scenarios. (B) SSIM of T1/T2/T1ρ against the reference images for the 14 simulation scenarios. The proposed method (motion-resolved) produces highest SSIM for all scenarios.
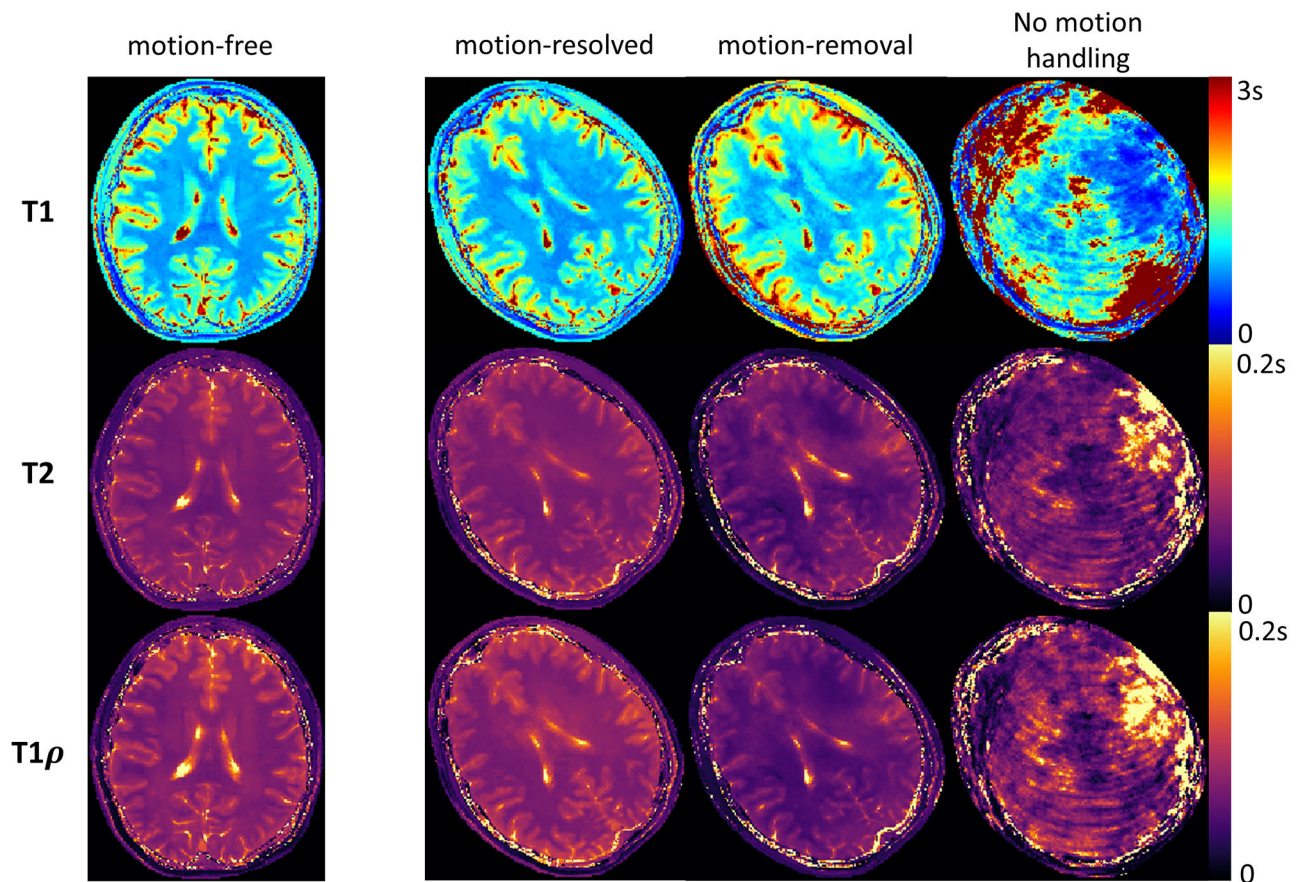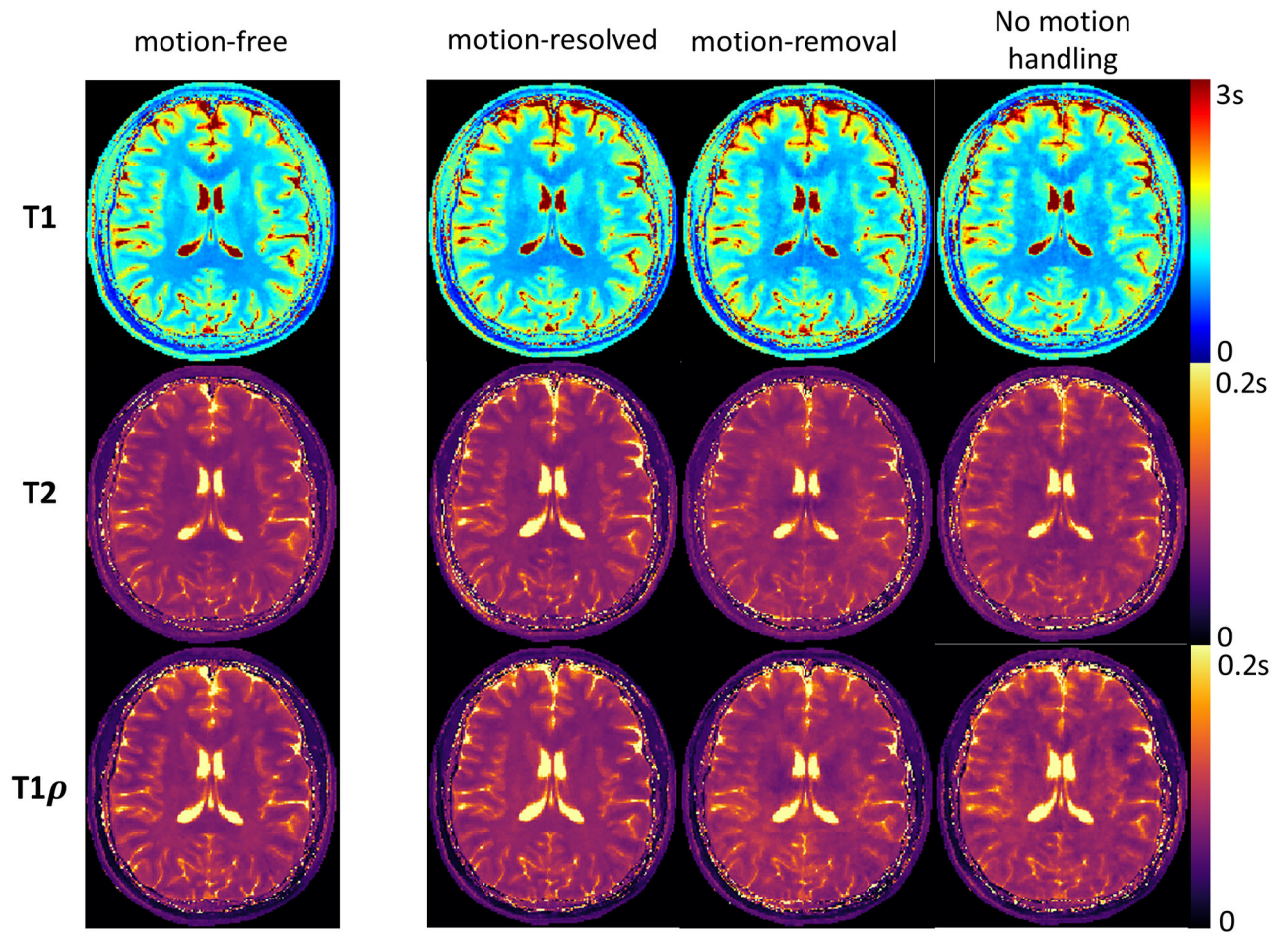
Figure 6.

In vivo T1/T2/T1ρ maps from one subject under large discrete motion. K_0=4 motion states were identified for this case. The 1st motion state was used for fitting. The motion-resolved solution produced clean T1/T2/T1ρ maps with sharp tissue structure. Notable blurring and ghosting artifacts were observed for no motion handling. Motion-removal produced substantially biased parameter maps with a loss of image features.
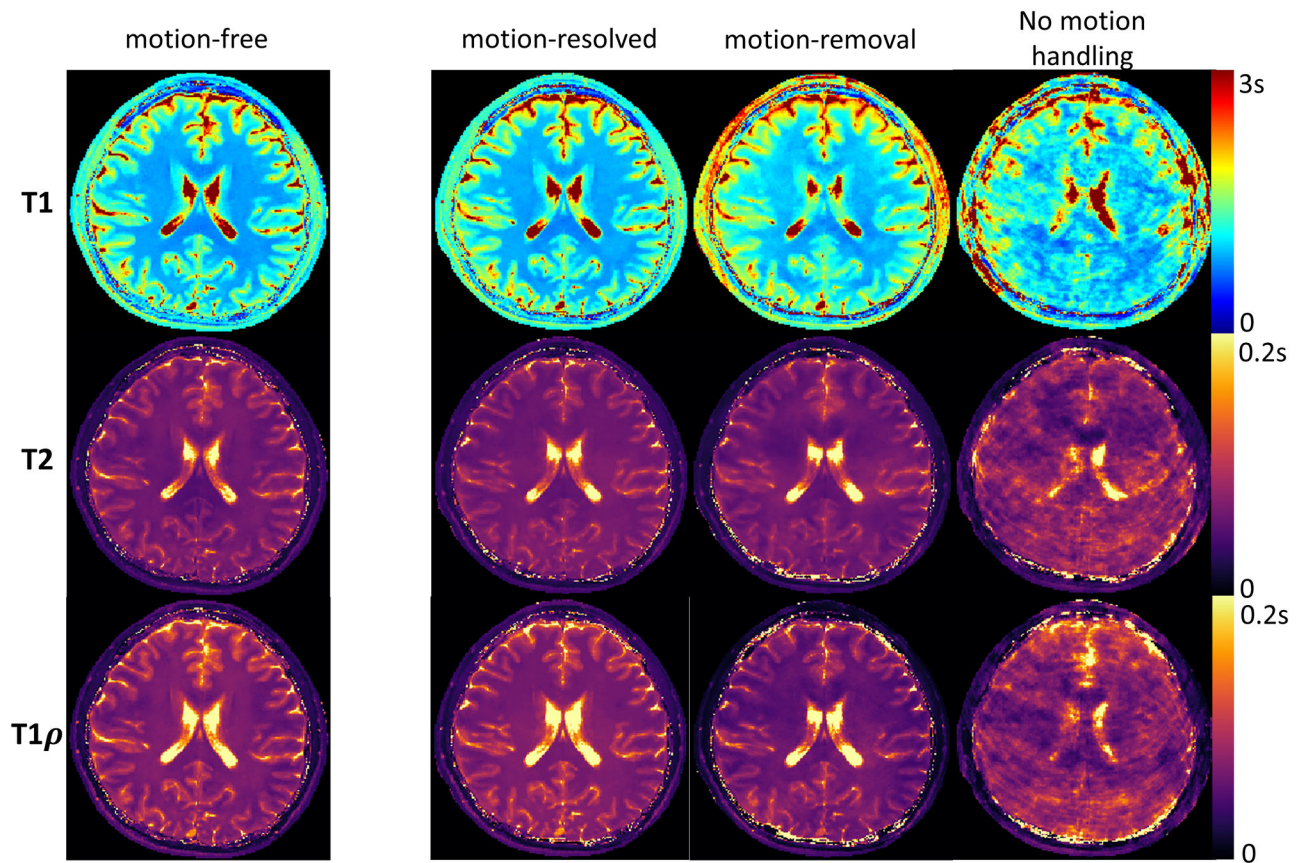
Figure 7.
In vivo T1/T2/T1ρ maps from one subject under "tremor-like" motion. K_0=6 motion states were identified for this case. The 4th motion state was used for fitting. The motion-resolved solution produced clean T1/T2/T1ρ maps with sharp tissue structure. Notable blurring and ghosting artifacts were observed for no motion handling. Motion-removal produced substantially biased parameter maps with a loss of image features.
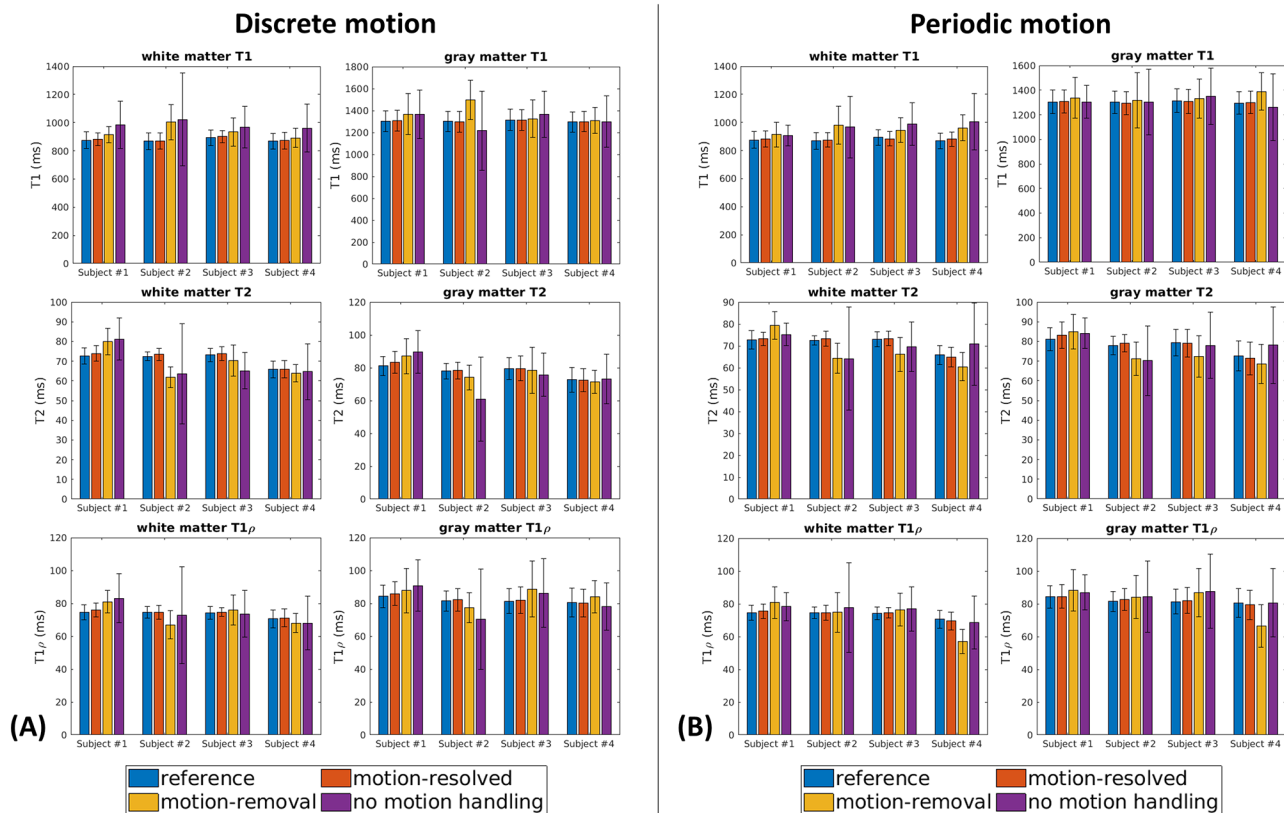
Figure 8.
In vivo T1/T2/T1ρ maps from one subject under "shaking" periodic motion. K_0=4 motion states were identified for this case. The 1st motion state was used for fitting. The motion-resolved solution produced clean T1/T2/T1ρ maps with sharp tissue structure. Motion artifacts and loss of image features were observed for no motion handling and motion-removal.

Figure 9.
In vivo T1/T2/T1ρ maps from one subject under "nodding" periodic motion. K_0=4 motion states were identified for this case. The 1st motion state was used for fitting. The motion-resolved solution produced clean T1/T2/T1ρ maps with sharp tissue structure. Blurring and ghosting artifacts were observed for no motion handling. Motion-removal produced parameter maps with substantial loss of image features and biased measurements.

Figure 10.
Quantitative T1/T2/T1ρ measurements of white matter and gray matter in four subjects with motion-free reference, no motion handling, motion-removal, and motion-resolved solution, in (A) discrete motion and (B) periodic motion experiments. The proposed method (motion-resolved) produced measurements closest to the reference, with matched mean values and standard deviation. No motion handling and motion-removal produced measurements with large biases and/or substantially deviated distributions, which corresponds to the motion artifacts and loss of image features of the parameter maps.